Elsevier Editorial System(tm) for Cement and Concrete Research
Manuscript Draft

Manuscript Number:

Title: Effective Properties of a Fly Ash Geopolymer: Synergistic Application of X-ray Synchrotron Tomography, Nanoindentation, and Homogenization Models

Article Type: Research Paper

Keywords: Alkali activated cement (D); Fly ash (D); Backscattered electron imaging (B); Micromechanics (C); X-ray tomography

Corresponding Author: Dr. Narayanan Neithalath, PhD

Corresponding Author's Institution: Arizona State University

First Author: Sumanta Das

Order of Authors: Sumanta Das; Pu Yang; Sudhanshu S Singh; James Mertens; Xianghui Xiao; Nikhilesh Chawla; Narayanan Neithalath, PhD

Abstract: Microstructural and micromechanical investigation of a fly ash-based geopolymer using: (i) synchrotron x-ray tomography (XRT) to determine the volume fraction and tortuosity of pores that are influential in fluid transport, (ii) mercury intrusion porosimetry (MIP) to capture the volume fraction of smaller pores, (iii) scanning electron microscopy (SEM) combined with multi-label thresholding to identify and characterize the solid phases in the microstructure, and (iv) nanoindentation to determine the component phase elastic properties using statistical deconvolution, is reported in this paper. The phase volume fractions and elastic properties are used in multi-step mean field homogenization (Mori-Tanaka and double inclusion) models to determine the homogenized macroscale elastic modulus of the composite. The homogenized elastic moduli are in good agreement with the flexural elastic modulus determined on macroscale paste beams. The combined use of microstructural and micromechanical characterization tools at multiple scales provides valuable information towards the material design of fly ash geopolymers.

Suggested Reviewers: Maria Juenger
UT Austin
mjuenger@mail.utexas.edu
Expertise in alkali activated systems

Mahmoud Reda Taha
U New Mexico
mrtaha@unm.edu
Expertise in nano and micromechanics

Nikhil Gupta
Polytechnic Univ. of NY
ngupta@poly.edu
Expertise in composite materials and characterization

Manuscript
Click here to download Manuscript: 3D characterization of FA Geopolymer - 04072015-Final.docx Click here to view linked References

Effective Properties of a Fly Ash Geopolymer: Synergistic Application of X-ray Synchrotron Tomography, Nanoindentation, and Homogenization Models

Sumanta Das[1], Pu Yang[1], Sudhanshu S. Singh[2], James C.E. Mertens[2], Xianghui Xiao[3], Nikhilesh Chawla[2], Narayanan Neithalath[1,*]

[1] School of Sustainable Engineering and the Built Environment, Arizona State University, Tempe, AZ, USA.

[2]Materials Science and Engineering, Arizona State University, Tempe, AZ, USA

[3]Advanced Photon Source, Argonne National Laboratory, Argonne, IL, USA

[*]Corresponding Author (Narayanan.Neithalath@asu.edu), Phone: 001-480-965-6023, Fax: 001-480-965-0557

ABSTRACT

Microstructural and micromechanical investigation of a fly ash-based geopolymer using: (i) synchrotron x-ray tomography (XRT) to determine the volume fraction and tortuosity of pores that are influential in fluid transport, (ii) mercury intrusion porosimetry (MIP) to capture the volume fraction of smaller pores, (iii) scanning electron microscopy (SEM) combined with multi-label thresholding to identify and characterize the solid phases in the microstructure, and (iv) nanoindentation to determine the component phase elastic properties using statistical deconvolution, is reported in this paper. The phase volume fractions and elastic properties are used in multi-step mean field homogenization (Mori-Tanaka and double inclusion) models to determine the homogenized macroscale elastic modulus of the composite. The homogenized elastic moduli are in good agreement with the flexural elastic modulus determined on macroscale paste beams. The combined use of microstructural and micromechanical characterization tools at multiple scales provides valuable information towards the material design of fly ash geopolymers.

Keywords: Alkali activated cement (D); Fly ash (D); Backscattered electron imaging (B); Micromechanics (C); X-ray tomography

1. INTRODUCTION

Alkali-activated materials provide an environmentally friendly alternative to conventional ordinary portland cement (OPC)-based binders that are prevalent in building and infrastructure construction. The use of industrial waste/by-product materials including fly ash, blast furnace slag, and clays can be activated using alkaline media to produce binders that have comparable or superior properties to those of OPC-based binders [1–5]. Geopolymers belong to the class of alkali-activated binders and are based on fly ash or metakaolin, resulting in an alkali aluminosilicate reaction product that is morphologically and behaviorally different from the calcium (alumino) silicate gels resulting from OPC hydration [6]. Several studies have evaluated the reaction kinetics, microstructure and mechanical properties of geopolymer systems in detail [4,5,7–9].

Similar to conventional OPC-based binders, geopolymeric systems are also inherently porous and heterogeneous, and display widely differing mechanical and durability properties depending on the material's microstructure. Thus, proper characterization of the pore-and-micro-structure is critical for a fundamental understanding of material behavior, as well as developing methods for adequate material design. Recent studies have evaluated the pore structure of fly ash geopolymers using mercury intrusion porosimetry (MIP) [9,10], which is a common method for conventional cementitious systems. An empirical approach to evaluate the fluid transport through fly ash geopolymer is reported in [10] where the Katz- Thompson model is used in conjunction with pore structural information from MIP [11–14]. Scanning electron microscopy (SEM) on two-dimensional images also are used for pore structure characterization [15,16]. The drawback of these methods (assumption of pore shapes, inconsistencies in pressurized mercury intrusion, having to deal with a large number of 2D images, inadequacy in determining phase connectivity information etc.) in probing the pore structure of heterogeneous materials can be alleviated to a large extent through the use of X-ray microtomographic (XRT or µCT) techniques. A few studies have evaluated the pore structure of cement-based and alkali-activated systems using this technique, thus helping to understand several characteristics such as distribution of air voids [17] spacing of fibers in 3D [18], leaching and sulfate attack in cement pastes [19,20], and pore network tortuosity [21,22].

While the pore structure of the material is important in dictating the transport behavior and, thus, the durability characteristics, the mechanical properties of a heterogeneous material are also influenced

significantly by the individual phase amounts (both solids and pore) and their properties. The individual phase elastic properties can be obtained through the use of nanoindentation experiments, as has been well documented for cement-based materials [23–26]. Micromechanical homogenization models are in-turn necessary to estimate the composite properties at the macro-scale. The response of the heterogeneous material at the micro-scale is averaged through analytical models, generally based on Eshelby's method [27–29], that replace the microscopically inhomogeneous strains and stresses by homogeneous values. The successful implementation of this approach demands accurate quantification of the phase volume fractions. The use of empirical models to determine the reaction product and pore volume fractions in highly heterogeneous systems containing multiple phases such as fly ash-based geopolymers is unlikely to yield satisfactory results. Moreover, it has been reported elsewhere that the classification and identification of different solid phases in the fly ash-based geopolymer using synchrotron XRT is challenging due to the low absorption contrast of different solid phases in the available x-ray energy range [22].

In this study, we have carried out a comprehensive investigation of a fly ash-based geopolymer based on 3D x-ray synchrotron imaging, nanoindentation of the individual constituents in the geopolymer, and micromechanics-based modeling of the mechanical properties. Synchrotron XRT is used to interrogate the pore structure using a pixel size of 0.74 µm, which is supplemented by MIP for smaller pore sizes. The 3D pore structural information from XRT is utilized in a numerical Stoke's solver [30–32] to develop a realistic assessment of the permeability of fly ash geopolymers. We have also conducted quantification of the microstructure using image segmentation and thresholding techniques. Multiple-phase quantification was accomplished using a multiple-thresholding image analysis procedure implemented on several high resolution backscattered SEM images. The quantified solid phase fractions are also validated through the frequency of occurrences of different solid phases in the statistical nanoindentation technique. The microscale properties are up-scaled using mean field homogenization schemes including Mori-Tanaka and double inclusion methods [28,29,33–37] to extract the homogenized Young's modulus, which is validated through macro-scale experiments. Linking the microstructure and micromechanical properties of a heterogeneous material, and using this information to predict the macroscopic mechanical performance, provides efficient means of optimizing the material design and mechanical behavior of fly ash-based geopolymers.

2. MATERIALS AND EXPERIMENTAL PROCEDURE

2.1 Materials and Mixture Proportions

A Class F fly ash conforming to ASTM C 618 was used as the starting material. The chemical composition of fly ash, determined using x-ray fluorescence is shown in Table 1. 8M NaOH solution was used to activate the fly ash. The alkaline solution was added to fly ash, and mixed for 4 minutes in a laboratory mixer. The mixtures were then filled in molds and subjected to heat curing in a laboratory oven at 60°C for 48 hours, in sealed conditions. This curing process was previously shown to provide a compressive strength of 25-30 MPa [2], which is commonly adopted for many types of structural concretes.

Table 1: Chemical composition and physical properties of fly ash

SiO_2	Al_2O_3	Fe_2O_3	CaO	MgO	SO_3	Na_2O	K_2O	LOI	Median particle size
58.4%	23.8%	4.19%	7.32%	1.11%	0.44%	1.43%	1.02%	0.5%	19 µm

2.2 Synchrotron X-ray Tomography

Synchrotron X-ray tomography (XRT) was performed at the 2-BM beamline of the Advanced Photon Source (APS) at Argonne National Laboratory. Details of APS beamline 2-BM have been described elsewhere [38,39]. A monochromatic beam with energy of approximately 27 keV was focused on samples of approximately 1.5 mm in size. The transmitted x-rays were converted to visible light using a LuAG:Ce scintillator screen coupled with an objective lens and CoolSnap K4 CCD camera to achieve a pixel size of 0.74 µm. 2D projections were acquired at angular increments of 0.12° over a range of 180°. The 2D projections were then reconstructed to 3D using Fast Fourier Transform (FFT)-based Gridrec algorithm [40–42]. XRT has been employed in the analysis of pore-structure of cementitious materials, and synchrotron microtomography is considered highly suitable for the evaluation of pore structure that is influential in dictating the transport properties and material durability [22,43–45].

2.3 Mercury Intrusion Porosimetry (MIP)

The pore structure of the fly ash-based geopolymer pastes was also evaluated using mercury intrusion porosimetry (MIP) to examine the pores in the smaller size ranges that was not able to be probed by XRT. A porosimeter that can detect minimum pore diameter of 0.0036 µm was employed for this study. This test was performed in two steps: (i) evacuation of gasses and filling the sample holder with mercury in the low-pressure run that increases the pressure from ambient to 345 kPa, and (ii) intrusion of mercury into the sample at high pressure (maximum pressure of 414 MPa). A solid–liquid (pore wall-mercury) contact angle of 130° and a mercury surface tension of 485 mN/m were used to interpret the results using the Washburn equation [14,46,47].

2.4 Nanoindentation

For nanoindentation, a cylindrical sample of 25 mm in diameter and 75 mm in height was prepared and heat cured at 60°C for 48 hours. A cubic piece with 4 mm sides was cut and polished to a 0.04 µm colloidal silica finish. The nanoindentation measurements were carried out on the polished sample in a commercial Nanoindenter (MTS Nanoindenter XP) using a Berkovich tip. Samples were mounted on aluminum stubs for nanoindentation testing using superglue. Indentations were carried out at initially at ~10 µm spacing in a grid on an area approximately 250 µm x 250 µm in size, which is considered representative for cementitious materials [22,48]. All the indentation locations were carefully selected prior to testing to ensure that the pores or cavities are not encountered in the process. Thus, the indentation experiments were carried out mostly on the solid phases, which resulted in very few spurious peaks in the modulus frequency distribution curves. The depth of penetration was chosen to be 500 nm which is smaller than the characteristic size of unreacted fly ash inclusions in order to avoid phase-interactions during penetration. Continuous stiffness measurement (CSM) technique [49–52] was employed here to measure the contact stiffness. While the traditional Oliver-Pharr methodology [53] measures the contact stiffness only at the point of unloading, the CSM technique allows measurement of contact stiffness at any point of the loading curve corresponding to any depth of penetration. CSM is accomplished by imposing a harmonic excitation of constant amplitude and frequency to the normally increasing load on the indenter. For any excitation frequency, the displacement response of the indenter and the phase angle are measured continuously as a function of the penetration depth. The contact stiffness, as a function of penetration depth, is obtained by solving for the in-phase and out-of phase portions of the response which are described in detail in [50]. Young's modulus for an individual indentation was measured as the average value over a depth range where both modulus and hardness were independent of depth. A constant Poisson's ratio of 0.20 was used in elastic modulus calculations since the effect of variation of Poisson's ratio in the range 0.18-0.22 has been reported to be insignificant for similar systems [26,37].

2.5 Scanning Electron Microscopy (SEM)

The plane polished sample was prepared as explained in the section on nanoindentation. The sample was imaged under a Philips XL30 field emission environmental scanning electron microscope (FESEM) in the backscattered mode to obtain high resolution micrographs that distinguishes different solid phases.

168 Several high resolution Images were obtained at different magnifications so that volume fractions of
169 different solid phases could be determined using a multi-label segmentation algorithm.

170 *2.6 Flexural Test on Geopolymer Beams*

171 Three-point bend tests were performed on prismatic beams of size 330 mm x 76 mm x 25 mm (span of
172 305 mm). Six replicate beams were tested. The beams were tested in a mid-span displacement-
173 controlled mode at a constant displacement rate of 0.004 mm/sec. The mid-span displacement was
174 measured continuously using a LVDT. The test was terminated at a center-point displacement value of
175 0.018 mm when the load reaches about 80% of the peak load which was determined previously from
176 simple flexural strength tests.

177 **3. RESULTS AND DISCUSSION**

178 *3.1 Multi-Scale Evaluation of the Pore- and Microstructure of Fly ash-based Geopolymer*

179 This section provides a detailed look into the pore- and micro-structure of the fly ash-based geopolymer
180 using several techniques to capture the effects at different length scales. It is well known that the pore-
181 and micro-structural features exert a significant influence on the mechanical and transport properties of
182 any porous material [14,54]. The pore network features (total and connected volume, critical pore size,
183 and tortuosity) and the distribution of the pore and solid phases are characterized using X-ray
184 microtomography (XRT), scanning electron microscopy (SEM), and mercury intrusion porosimetry (MIP).
185 The pore structural features are used to predict fluid transport through the porous material while the
186 phase volumes and micromechanical phase properties are employed in the prediction of homogenized
187 composite properties as elucidated in a later section.

188 <u>3.1.1 Microstructure of alkali-activated fly ash from backscattered SEM</u>

189 Figure 1 shows representative backscattered SEM micrographs of the geopolymer paste after 2 days of
190 sealed heat curing at 60°C. The reaction product in NaOH-activated aluminosilicate materials such as fly
191 ash and metakaolin is a sodium aluminosilicate (N-A-S-H) gel, the characteristics of which have been
192 extensively reported [9,55,56]. These micrographs demonstrate the presence of unreacted/partially
193 reacted fly ash, reaction product (N-A-S-H) and the pore phase in the fly ash-based geopolymer. N-A-S-H
194 gel (brighter grey phase) is found around the fly ash particles as well as uniformly distributed in the
195 microstructure. The micrographs also show unreacted rounded fly ash particles and partially reacted fly
196 ash particles. In addition, the pore phase (darker phase) can also be distinguished, both in the N-A-S-H

gel as well as within some fly ash particles (cenospheres) [10,22]. While a small fraction of the partially reacted fly ash particles retain their rounded shape, there are also particles that have undergone non-uniform dissolution on their surfaces.

3.1.2 3D Characterization and quantification of component phases using Synchrotron X-Ray Tomography (XRT)

Synchrotron XRT provides valuable 3D information on the pore structure of random heterogeneous materials, which is yet unavailable through other commonly adopted methods, enabling the prediction of transport properties and thus the material durability. In order to facilitate efficient computation, cubic volumes of interest of sizes ranging from 50^3 voxels to 400^3 voxels were extracted from different areas of the original synchrotron XRT reconstruction corresponding to the sample size used, in order to determine the influence of the size of the representative volume element (RVE) on the accuracy of the extracted pore structure features. Representative microstructures for the selected RVE sizes (50^3, 100^3, 200^3 and 300^3 voxels) are shown in Figures 2(a1 to d1). The process of quantification of phase volumes from the representative microstructures requires accurate segmentation. Segmentation involves selection of threshold greyscale values to distinguish between different phases present in the material. Phase segmentation in heterogeneous materials such as cementitious systems with minimal greyscale contrast between the component phases is a difficult problem, and is an area of ongoing research [22]. For fly ash-based geopolymers, the difficulty is exacerbated by the presence of partially reacted/unreacted fly ash particles, compositional aspects of fly ash particles that make some appear brighter and some less so, and the relative densities of the N-A-S-H gel based on its location of formation in the microstructure (closer to the fly ash or diffused away from it). A comprehensive discussion on such aspects can be found in [22].

In this study, the phase segmentation process was implemented in Avizo Fire™ software package that employs advanced filters and operators for image processing and analysis[#]. First, a transition point (in the grey scale histogram) where a small increment in the threshold value causes a sharp change in the detected phase quantities, which has traditionally been used for phase identification [22,44], is employed. However, this global thresholding method alone was found not completely reliable for the fly ash-based geopolymer systems by virtue of a wide range of greyscale intensities and the presence of pores within some of the fly ash particles. Similar observations are reported elsewhere [22]. Therefore, the transition point-based thresholding is augmented with the application of appropriate discrete

[#] This does not imply an endorsement of the software package.

thresholding in the microstructure to obtain the most realistic representation of known microstructural features such as rounded unreacted fly ash particles, cenospheres, and N-A-S-H gel around partially reacted fly ash particles. The discrete operations were carried out for 2D images in the 3D stack using routines implemented in the analysis software. Figures 2(a2-d2) show the thresholded microstructures corresponding to the different RVE sizes, where the segmentation algorithm described above has been implemented to separate the pore and solid phases.

Figure 3 depicts the influence of the RVE size on porosity and tortuosity of the fly ash-based geopolymer. A number of RVEs of different sizes were extracted from different regions of the original 3D XRT image. For the RVE sizes of 50^3, 100^3, 200^3, 300^3 and 400^3 voxels, the number of 3D images analyzed were 40, 20, 10, 5 and 4 respectively. Here, segmented porosity refers to the extracted porosity obtained after segmentation and it includes all the connected and isolated pores (e.g., fly ash cenospheres) in the microstructure. On the other hand, connected porosity is the pore cluster that percolates in all three orthogonal directions. While the total volumetric porosity influences the mechanical properties of the material, the connected porosity significantly influences the durability characteristics of the material such as its resistance to moisture and ionic transport. The percolated porosity and tortuosity is calculated using a pore-centroidal algorithm implemented in Avizo Fire™. The algorithm involves determination of the pore-network centroids within each slice, and then tracking its movement between each slice in all three directions. The tortuosity is calculated by dividing the cumulative centroidal lengths by the edge length of the RVE in the corresponding directions [57]. The summation of total volume of such connected pathways is divided by the total sample volume to obtain the connected porosity.

Figure 3(a) shows the influence of the RVE size on the segmented and connected porosities of the geopolymer paste. The average segmented porosity remains relatively invariant of the RVE size even though the variability is much larger, as expected, when smaller RVEs are used. The average connected porosity decreases slightly as the RVE size is increased from 50^3 to 200^3 voxels; however no further change is observed with increasing size. For RVE sizes of 300^3 and 400^3 voxels, the variability in the segmented and connected porosities is very low, signifying the applicability of such RVE sizes for phase quantification and property estimation. It is also noted from Figure 3(a) that the connected porosity is significantly lower than the segmented (overall) porosity, attributed to the hollow fly ash particles. Figure 3(b) depicts the influence of RVE size on tortuosity. The tortuosity is observed to increase with an increase in the RVE size, showing that it is much more sensitive to the RVE size than the porosity. For

smaller RVEs, the connected paths are shorter and are not representative of the intricacies of the pore structure. A certain threshold size appears to be necessary (~300^3 voxels in this case) to capture the accurate tortuosity of the pore structure. The values of tortuosity obtained here are lower than those reported for fly ash-based geopolymers in other studies [22], likely attributable to the differences in processing and curing parameters, and the algorithms implemented. Here also, variability in determined tortuosity decreases with increase in RVE size. Results of this comprehensive evaluation of size-dependence establishes that, for the fly ash-based geopolymers, an RVE size of 300^3-400^3 voxels is sufficient to eliminate finite-size error, in line with what is reported in [22]. A RVE of 300^3 voxels (222^3 μm^3) has been chosen here for further quantification of permeability as a compromise between accuracy and computational demand.

Figure 4 demonstrates the application of the segmentation procedure that employs discrete thresholding based on known microstructural features for multiple phases. Figure 4(a) is the original 300^3 voxel image from XRT, while Figure 4(b) shows the pore (red) and solid (grey) phases segmented using the procedure similar to the one described in the discussion relating to Figure 2. Figure 4(c) exhibits the 3D XRT image after multiple thresholding. Here three phases (pores in red, fly ash in yellow, and the reaction product in grey) are shown. The unreacted and partially reacted fly ash phases could not be separated due to indistinguishable greyscale intensities. While the sequential thresholding method could provide an indication of the relative quantities of these phases, a closer observation to compare several random thresholded 2D slices with the actual XRT images showed that some fly ash particles were labeled as N-A-S-H gel while the actual gel around the fly ash particles in some images were labeled as part of fly ash. Thus the classification and identification of such phases using method of edge detection in synchrotron XRT images is challenging due to low absorption contrast in available x-ray energy range. Hence the use of synchrotron XRT data is limited to quantification of 3D pore structure in this study. A quantification of volume fractions of distinct solid phases, towards mechanical property prediction, is carried out using several high resolution backscattered SEM images on plane polished samples which are presented in detail in a forthcoming section.

3.1.3 Pore structure evaluation using MIP and comparison with XRT results

As described earlier, XRT reconstruction allows observation and quantification of features using a voxel size of 0.74 µm. However, it is well known that there is a significant fraction of pores smaller than this size in cementitious and geopolymeric systems. Thus, mercury intrusion porosimetry (MIP) is used to evaluate the pore structure in the pore size range of 0.0036 µm-to-10 µm to complement the XRT

studies that interrogated sizes in the range of 0.74 µm-to-50 µm. Figure 5(a) shows cumulative mercury intrusion curve for the alkali-activated fly ash. Even though the MIP porosity obtained here (~32%) and the segmented volumetric porosity quantified using reconstructed XRT images (Figure 3a) are similar, it is nothing more than a coincidence because both these techniques operate at different pore size ranges. Figure 5(a) shows dominant contribution of pores of sub-micron size (0.0036 µm-to-1 µm) to the overall porosity of the material. Figures 5(b) and (c) segregates the pore size distribution quantified by XRT using a 300^3 voxel RVE at lower (0.75 µm-to-25 µm) and upper (25 µm-to-50 µm) ranges of XRT detection. The frequency distribution figures reveal that the number of smaller pores, especially in the range of 4 µm-to-12 µm, are significantly higher than the larger pores. While a significant amount of smaller pores (0.74 µm-to-12 µm) are most likely to contribute to the connected/percolated porosity, the bigger pores are mostly observed to be isolated and a significant fraction of those are attributed to the hollow fly ash particles. Figure 5(d) shows a comparison of the two pore quantification approaches in terms of the contribution of different pore size ranges to the overall porosity of the material. There is a zone of convergence in the range of 0.74 µm-to-5 µm where both the methods quantify similar pore volume fractions. Pores in the size range of 0.0036 µm-to-0.05 µm are found to be the dominant contributors to the overall MIP porosity (40% of the overall porosity). These small pores can be safely considered as the fine gel pores belonging to the N-A-S-H structure. XRT dataset shows that pores in the size range of 5 µm-to-24 µm contribute the most to the overall segmented porosity. From a viewpoint of material durability, it is the larger pores that contribute to the rapid transport of moisture and ionic species, a significant portion of which can be quantified using XRT. The inherent disadvantages of MIP with respect to identification of pore size distributions in cementitious systems, which is well-documented [58,59] should also be accounted for.

3.2 Predicting Permeability from XRT Reconstructed 3D Microstructures

The intrinsic permeability is a measure of relative ease with which a fluid can be transported through a porous media under a potential gradient. Models have been developed to predict the permeability of porous materials from their pore structure features [11–14,30–32]. Among them, the Navier-Stoke's [30–32] and Katz-Thompson models [11–13] are widely used and are employed here to evaluate the intrinsic permeability of the fly ash-based geopolymer from the pore structure features. The Navier-Stoke's model is applied on the XRT data and a variant of the Katz-Thompson model on the MIP data [13,14]. A pressure gradient of one unit per voxel is employed in the direction desired (X, Y, or Z) to induce the flow through the RVE. A finite volume method to solve the simplified Navier-Stoke's

equations for the velocity and pressure fields (Equation 1) is used along with an artificial compressibility relaxation algorithm [30–32].

$$\nabla u = 0$$
$$\mu \nabla^2 u - \nabla P = 0 \quad [1]$$

In the above equation, P is the pressure (Pa), u is velocity (m/s), and μ is the viscosity (Pa.s). The intrinsic permeability (k) is calculated by volume averaging the local fluid velocity and applying the Darcy's equation:

$$u = -\frac{k}{\eta}\frac{\Delta P}{L} \quad [2]$$

Here, ΔP is the pressure difference and L is the specimen length. The permeability is calculated in all three directions in an RVE of size 300^3 voxels (222^3 μm^3) using Stoke's solver. Five different RVEs of size 300^3 voxels are sampled from different regions of the original XRT data for permeability prediction. Figure 6 reports the computed permeability in three orthogonal directions, which are very close to each other. The predicted permeability is approximately 5 x 10^{-14} m^2. While experimental intrinsic permeability data for fly ash geopolymers are not readily available, the results reported for conventional cementitious systems span a wide range [60]. The use of Stokes solver on 3D reconstructed structure of transmission X-ray microscopic images of a cement paste having a porosity of 23% provided permeability in the range of 10^{-18} to 10^{-17} m^2, while values in the same range are reported for low porosity (~10%) cement paste specimens in [61]. For 3D cement paste microstructures simulated using two different methods, at 1 μm pixel size and having a porosity of 27%, a permeability of 7-to-8 x 10^{-15} m^2 has been obtained through the use of Lattice-Boltzmann method and Navier-Stoke's equation [48,60]. Thus, it appears that the permeability of 5 x 10^{-14} m^2 obtained for the fly ash-based geopolymer in this study is reasonable, considering that the porosity of the system, as obtained from XRT is about 32%. It also needs to be mentioned that the computed permeability is highly dependent on the pore tortuosity. For the system considered, the tortuosity is relatively low (~2.5), likely due to the low levels of fly ash reaction.

It is also instructive to use the Katz-Thompson (K-T) model to determine the permeability based on a characteristic length of the pore structure that can be obtained from MIP [11–14]. In contrast to the widely used K-T model that employs the normalized electrical conductivity and a characteristic length (usually, the percolating pore size), a simplified K-T model includes only the characteristic length terms extractable from MIP to predict the permeability, which is given as [14]:

$$k = \frac{1}{89}(L_{\max})^2(\frac{L_{\max}}{L_c})\phi S(L_{\max}) \quad [3]$$

Here, L_c is characteristic length or the pore diameter corresponding to threshold pressure (the pressure corresponding to point of inflection in the rapidly rising range of the cumulative mercury intrusion curve), L_{max} is the pore diameter at which the hydraulic conductance is maximum, ϕ is the porosity, and $S(L_{\max})$ is the fraction of volume of connected pore space composed of pores of size L_{max} or larger. The permeability predicted by the modified K-T model is 5.2 x 10^{-16} m^2, which is similar to that of a plain cement paste at 50% hydration [61]. The application of a similar method on alkali activated fly ash pastes of similar porosity predicted an intrinsic permeability in the range of 10^{-17} m^2 [10], thus corroborating the results reported here. The MIP-based permeability is about two orders of magnitude lower than that computed from the XRT based 3D structure, which is not surprising considering the lower range of pore sizes accessed through MIP.

3.3 Micromechanical Behavior of the Fly Ash-Based Geopolymer and Modeling

The previous section examined the microstructure of alkali activated fly ash at different length scales using XRT, SEM, and MIP, and employed microstructure-based predictive tools for transport properties. In this section, the mechanical performance of the individual phases in the geopolymer system is evaluated using nanoindentation. The individual phase responses are homogenized using established micromechanical theories to obtain predictions of elastic properties of the geopolymer, which is then validated through macroscale tests.

3.3.1 Nanoindentation for component phase elastic properties

For the classification of different phases present in alkali-activated fly ash paste and a quantification of Young's modulus of different phases, a statistically significant number of indentations were performed on carefully chosen solid regions in the paste (based on a 250 μm x 250 μm grid) through microscopic observation of the indentation locations. This ensures that the material microstructure within each interaction volume can be estimated with a high degree of confidence, and the validity of isotropicity and homogeneity within the interaction volume can be ensured, which is absolutely important in interpreting indentation results of heterogeneous materials [62]. Penetration depths of up to 500 nm were employed to ensure that the measured elastic properties are not influenced by the sample preparation process that could introduce surface effects. Representative load-penetration depth plots to identify the phases of differing stiffness (the methodology to assign phases is explained below) are

presented in Figure 7(a). The elastic modulus values as a function of penetration depth were calculated using the CSM technique described in the experimental program section and representative curves are shown in Figure 7(b). For all the measurements, average elastic modulus in a penetration depth range of 100-to-200 nm is computed (since the E is invariant of depth in this range) and used for further analysis. The mean Young's modulus, along with a phase quantification procedure described later, is used in a homogenization scheme for quantification of bulk Young's modulus of the fly ash-based geopolymer.

The experimental probability density functions (PDFs) are obtained from experimental measurements by employing a bin size (b) of 1 GPa which is presented in Figure 8(a) (symbols). Four characteristic peaks are observed in the histogram. Statistical deconvolution [37,63,64] is applied to the elastic modulus histogram to obtain individual phase elastic properties. Assuming Gaussian distribution for all the four phases (which is a reasonable assumption based on the data points in Figure 8(a)), the theoretical probability distribution function (pdf) is given as:

$$C(x) = \sum_{r=1}^{4} f_r \frac{1}{\sqrt{2\pi s_r^2}} \exp \frac{-(x-\mu_r)^2}{2s_r^2} \qquad [4]$$

In Equation 4, x represents the elastic modulus, f_r is the volume fraction of the rth phase, and μ_r and s_r are the mean and standard deviation of the rth phase. The deconvolution algorithm involves random seeding using a Monte Carlo simulation and minimization of quadratic deviations between the experimental and theoretical PDFs to find the relevant parameters for the Gaussian distribution functions. More details on the deconvolution algorithms can be found in [37,63,64]. The sum of the deconvoluted peaks is identified using the solid line in Figure 8(a).

Figure 8(b) shows the deconvoluted PDFs for the four different phases. SEM observation of the microstructure at the indented locations, along with an understanding of the phases present in fly ash-based geopolymers based on past studies, was used for the assignment of the deconvoluted peaks to the individual peaks. The solid phase with the highest elastic modulus can be attributed to the unreacted fly ash present in the matrix, while the phase with the lowest elastic modulus can be attributed to the N-A-S-H gel that is formed through diffusion of the ionic species and gel precipitation in the empty spaces in the microstructure. This gel is intrinsically nanoporous, but since an estimation of the gel porosity is tedious, the measured elastic modulus is considered to be the value for the N-A-S-H gel considered virtually to be a "solid". Similar values of elastic moduli for these phases have been reported in previous studies [64,65]. A comprehensive evaluation of the microstructure was carried out

towards attributing the component microstructural phases to the two remaining deconvoluted peaks of the elastic modulus distribution. The peak corresponding to the lower among the two peaks corresponds to the fly ash particles that have reacted partially, and the reaction products are retained around or close to the particles, thus providing them with a higher elastic modulus than the N-A-S-H gel that has diffused away from the particles. These phases are referred to as partially reacted fly ash. Similar values for this phase have been reported in [64,65]. The identification of the other peak was somewhat difficult. The indentation locations were mostly on fly ash particles and it is hypothesized here that the peak could be attributed to particles with some reaction products on the surface, or to unreacted fly ash particles with cavities, many of which are observed in the micrographs. Image analysis on backscattered SEM to quantify these phases have been reported in a forthcoming section. The deconvolution results are presented in Table 2.

Table 2: Elastic properties of individual solid phases and their frequency of occurrence in the microstructure as determined by nanoindentation

	N-A-S-H gel (Phase 1)	Partially activated fly ash (Phase 2)	Partially activated fly ash or fly ash with cavities (Phase 3)	Unreacted fly ash (Phase 4)
Elastic modulus [GPa]	16.3 ± 4.1	32.4 ± 5.1	43.7 ± 2.8	72.0 ± 6.8
Frequency of occurrence (in the solid phases)	60.4%	22%	8.2%	9.4%

3.3.2 Mean-field homogenization methods for elastic property prediction

Homogenization procedures are applied to heterogeneous materials such as cementitious systems to determine the homogenized elastic properties using individual phase properties (e.g., determined from nanoindentation) and phase amounts (e.g., determined from XRT or SEM) to be used in material design. Mean field homogenization techniques are based on Eshelby's tensors [27] to determine the average stresses and strains in inclusions embedded in an elastic matrix. Two homogenization methods are employed in this study: (1) Mori-Tanaka scheme [28] and (2) double inclusion model [29]. The analytical schemes of these models have been well documented [28,29,33–37].

Mori-Tanaka method has been used for determination of effective properties in cement-based materials [26,36,37]. It considers a discrete spherical inclusion embedded in an infinitely extended homogeneous

reference medium (matrix). In this method, the homogenized bulk and shear moduli for two-phase materials can be quantified from the individual phase properties as given in Equation 5. The individual phase shear and bulk moduli are obtained from their elastic modulus and Poisson's ratio.

$$k_{\text{hom}} = \frac{f_i k_i (1+\alpha_{ref}.(\frac{k_i}{k_{ref}}-1))^{-1}}{f_i (1+\alpha_{ref}.(\frac{k_i}{k_{ref}}-1))^{-1}} \quad [5a]$$

$$\mu_{\text{hom}} = \frac{f_i \mu_i (1+\beta_{ref}.(\frac{\mu_i}{\mu_{ref}}-1))^{-1}}{f_i (1+\beta_{ref}.(\frac{\mu_i}{\mu_{ref}}-1))^{-1}} \quad [5b]$$

Here i is the number of inclusions; f_i is the volume fraction of ith inclusion; k_i and k_{ref} are the bulk moduli for the ith inclusion and reference medium respectively; μ_i and μ_{ref} are shear moduli for the ith inclusion and reference medium respectively and α_{ref} and β_{ref} are given in Equation 6 [37,63]. A detailed methodology to extract the component volume fractions is presented in the following section.

$$\alpha_{ref} = \frac{3k_{ref}}{3k_{ref} + 4\mu_{ref}} \quad [6a]$$

$$\beta_{ref} = \frac{6k_{ref} + 12\mu_{ref}}{15k_{ref} + 20\mu_{ref}} \quad [6b]$$

From homogenized bulk and shear modulus, the homogenized Young's modulus can be calculated as [37,63]:

$$E_{\text{hom}} = \frac{9k_{\text{hom}}.\mu_{\text{hom}}}{3k_{\text{hom}} + \mu_{\text{hom}}} \quad [7]$$

A three-step homogenization is performed as shown in Figure 9(a). In Step I, unreacted fly ash is the inclusion in a homogeneous N-A-S-H matrix, and these two phases are homogenized. In Step II, partly reacted fly ash is incorporated into the homogenized medium. In Step III, pores are added as inclusions to the homogenized medium from Step II.

While the Mori-Tanaka model consists of an ellipsoidal inclusion in an infinitely extended homogeneous reference medium, a modification implemented in the double inclusion model consists of an ellipsoidal inclusion of stiffness $\tilde{S}_{I-1}$ embedded in another ellipsoidal matrix of stiffness $\tilde{S}_{I-2}$, which is further embedded in an infinitely extended homogeneous medium of stiffness $\tilde{S}$ [35,36] as shown in Figure 9(b). This method accounts for the inclusion-inclusion interaction in addition to matrix-inclusion interactions considered in the Mori-Tanaka approach [29]. The average elastic moduli can be calculated as:

$$\bar{\tilde{S}} = [\tilde{S}^{-1} + f_1\alpha + f_2\beta]^{-1} \qquad [8]$$

In the above equation, f_1 and f_2 are volume fractions of two inclusion phases, and α and β are functions of f_1 and f_2 and the Eshelby's tensors $\tilde{S}$, $\tilde{S}_{I-1}$, and $\tilde{S}_{I-2}$. Detailed derivation and analysis procedure are described in [29,35,36]. In line with microstructural observations, here unreacted fly ash is considered to be embedded in partially reacted fly ash, and the double inclusion of unreacted and partially reacted fly ash particle is embedded in an infinitely extended N-A-S-H gel. The obtained homogeneous property of the solid phase is homogenized with the pore phase using the Mori-Tanaka scheme to obtain the overall homogenized Young's modulus, as shown in Figure 9(b).

3.3.3 Determination of volume fractions to be used in the homogenization schemes

The mean-field homogenization schemes that are used for the estimation of macro-level properties requires precise input in terms of phase volume fractions. It was mentioned earlier that synchrotron XRT delivers good contrast between the solid and the pore phases (at the resolution considered), which makes it an attractive tool for 3D characterization of the pore structure. Thus, the overall pore volume determined from XRT is directly used in the homogenization schemes for elastic property prediction. However, identification and quantification of different solid phases in the fly ash-based geopolymer systems (especially distinguishing partially reacted and unreacted fly ash phases) is challenging for reasons described earlier in this paper. Hence, the XRT information is supplemented in this study through the determination of volume fractions of different solid phases using two approaches: (i) frequency of occurrences of different phases using statistical nanoindentation technique (Figure 8b, where the integrated intensities correspond to the volume fraction of the phase assigned to that peak), and (ii) multi-label thresholding (combination of global thresholding using a transition point approach

477 and discrete thresholding considering known microstructural features of fly ash-based geopolymers) of
478 several high resolution backscattered SEM images. The multi-label thresholding was selected based on
479 global thresholding and/or based on known microstructural features such as: (a) unreacted fly ash
480 particles which are rounded and without any reaction products surrounding them, (b) partially (in some
481 cases, almost fully) reacted fly ash where the particles have reacted to form the gel and the reaction
482 products are retained around or close to the particles, (c) pores both in the matrix as well as part of the
483 fly ash particles (cenospheres) which are generally distinguishable easily through global thresholding
484 method using a transition point approach, and (d) N-A-S-H gel which is the remaining solid phase after
485 considering (a) and (b). Figures 10 (a) and (b) show a representative micrograph and its color
486 thresholded version respectively, showing all the distinct phases.

487 The nanoindentation-based approach does not quantify the volume fraction of pores since the pores
488 were avoided while selecting the indentation locations prior to testing. Thus the porosity obtained from
489 3D synchrotron XRT using the analysis scheme described earlier was used to infer the volume fraction of
490 pores in the bulk material. It needs to be noted that the smaller peak in the deconvoluted spectrum of
491 the nanoindentation results that was attributed to partly reacted fly ash/hollow fly ash particles (Figure
492 8b) could not be isolated with a desirable degree of confidence based on careful observation of
493 micrographs. Hence the corresponding volume fraction obtained for this phase was attributed
494 completely either to the partly reacted fly ash, or to the hollow fly ash particles during the analysis. In
495 other words, in the micromechanical homogenization scheme, this volume was added to that of partially
496 reacted fly ash or to that of unreacted fly ash for convenience, thereby effectively reducing a four-phase
497 solid to a three-phase solid as shown in Figures 9(a) and (b). It was found that attributing this phase to
498 the unreacted fly ash provided better predictions of the elastic modulus of the geopolymer paste even
499 though the differences were not large. The volume fraction of pores, quantified by several 2D high-
500 resolution SEM images, is found to be similar to the volume fraction quantified using image analysis on
501 reconstructed XRT images, which is not surprising because the SEM resolution is also limited to < 1 μm.
502 Thus, the smaller gel pores, which will be a part of N-A-S-H gel is not considered. Figure 10(c) shows the
503 phase volume fractions extracted, demonstrating a good agreement between both the methods. The
504 adequacy of supplementing 3D XRT data with a nanoindentation-based approach or a microstructure-
505 based discrete multi-label thresholding approach in quantifying volume fractions of component phases
506 in heterogeneous porous materials is evident from this figure.

507 <u>3.3.4 Homogenized elastic modulus and comparison with macro scale experiments</u>

Table 3 shows the homogenized Young's modulus for fly ash-based geopolymer pastes computed using the Mori-Tanaka approach and the double inclusion method. A comparison of homogenized elastic moduli based on phase volume fractions predicted by the SEM and nanoindentation-based approaches are also provided. Table 3 also shows the macroscale flexural elastic modulus of the pastes determined from three-point bend tests on geopolymer pastes. The tensile elastic modulus was extracted from the flexural load-deflection data using a moment-curvature-based inverse analysis methodology described in detail in [66,67], which is also shown in Table 3.

The macro-scale estimates of elastic modulus are in good agreement with those predicted using mean field microstructural homogenization. Mori-Tanaka approach provides a higher value of Young's modulus as compared to double inclusion method, because of the inter-inclusion interactions not being considered. The double inclusion model captures the heterogeneity of fly ash-based geopolymer more accurately, especially with its capability to consider reaction products around fly ash particles. Results of this comprehensive study establish the material property-microstructure link for fly ash-based geopolymers using a combination of synchrotron XRT, statistical nanoindentation and mean-field homogenization models.

Table 3: Homogenized elastic modulus and the experimental values from flexural test on bulk specimens.

Homogenized elastic modulus (GPa)				Macro-scale Young's modulus from experiments (GPa)	
Volume fractions from SEM		Volume fractions nanoindentation			
Mori-Tanaka	Double inclusion	Mori-Tanaka	Double inclusion	Flexural	Tensile
16.7 ± 2.9	15.1 ± 2.1	17.5	15.6	14.7 ± 0.7	14.9 ± 0.7

4. CONCLUSIONS

A comprehensive characterization of the pore- and micro-structure of a fly ash-based geopolymer has been reported here. Pore structure-based fluid transport prediction, determination of the elastic properties of solid microstructural phases using nanoindentation, and the use of homogenization models to predict the bulk elastic properties were detailed. Synchrotron XRT was used to extract the 3D information of the pore structure (total and percolated pore volume and tortuosity). The influence of the size of the RVE on the total pore volume and tortuosity have been brought out. The XRT data showed that pores in the size range 10 µm-to-20 µm contributes the most to the total porosity. A detailed comparison of pore structure features extracted using XRT and mercury intrusion porosimetry

(MIP) showed that the two methods determine comparable pore volumes only in the 0.75 µm-to-5 µm size range. The combination of MIP and XRT facilitates a complete characterization of the pore structure of fly ash-based geopolymers. The 3D microstructure was used in a computational implementation of Navier-Stoke's model to predict the permeability of the fly ash-based geopolymer.

A multi-label thresholding method was implemented on several high resolution SEM images for identification and quantification of solid phase volume fractions. The phase volumes thus calculated were also validated through frequency of occurrences of different solid phases from statistical nanoindentation. The individual phase elastic properties determined using nanoindentation along with the pore and solid phase volume fractions were used in multi-step micromechanical mean-field homogenization models to determine the homogenized Young's modulus of the composite. The homogenized Young's modulus, especially the one determined using the double inclusion method, was found to be in good agreement with the experimental macro-scale Young's modulus. This was attributed to the capability of the double inclusion method to accurately capture the microstructural intricacies of fly ash-based geopolymer pastes. This study, linking the microstructure and properties of a highly heterogeneous material (at the microscale), and the use of up-scaling models to predict the bulk elastic response, is expected to lead to better material design of fly ash-based geopolymers, which currently relies greatly on experimentally obtained bulk mechanical response only.

5. ACKNOWLEDGEMENTS

The authors gratefully acknowledge the National Science Foundation (NSF) for the partial support for this research (CMMI: 1068985 and CMMI: 1353170). This research was conducted in the Laboratory for the Science of Sustainable Infrastructural Materials, the Structural Engineering Laboratory, the Mechanical Behavior of Materials Facility, and 4D Materials Science Laboratory at Arizona State University and the supports that have made these laboratories possible are acknowledged. The 2-BM beamline of the Advanced Photon Source (APS) at Argonne National Laboratory is also acknowledged. The contents of this paper reflect the views of the authors who are responsible for the facts and accuracy of the data presented herein, and do not necessarily reflect the views and policies of the funding agency, nor do the contents constitute a standard, specification, or a regulation.

6. REFERENCES

[1] M.C.G. Juenger, F. Winnefeld, J.L. Provis, J.H. Ideker, Advances in alternative cementitious binders, Cem. Concr. Res. 41 (2011) 1232–1243.

[2] D. Ravikumar, S. Peethamparan, N. Neithalath, Structure and strength of NaOH activated concretes containing fly ash or GGBFS as the sole binder, Cem. Concr. Compos. 32 (2010) 399–410.
[3] S. Das, B. Souliman, D. Stone, N. Neithalath, Synthesis and Properties of a Novel Structural Binder Utilizing the Chemistry of Iron Carbonation, ACS Appl. Mater. Interfaces. 6 (2014) 8295–8304.
[4] S. Chithiraputhiran, N. Neithalath, Isothermal reaction kinetics and temperature dependence of alkali activation of slag, fly ash and their blends, Constr. Build. Mater. 45 (2013) 233–242.
[5] J.G. Jang, N.K. Lee, H.K. Lee, Fresh and hardened properties of alkali-activated fly ash/slag pastes with superplasticizers, Constr. Build. Mater. 50 (2014) 169–176.
[6] I. Lecomte, C. Henrist, M. Liégeois, F. Maseri, A. Rulmont, R. Cloots, (Micro)-structural comparison between geopolymers, alkali-activated slag cement and Portland cement, J. Eur. Ceram. Soc. 26 (2006) 3789–3797.
[7] M. Catauro, F. Bollino, F. Papale, G. Lamanna, Investigation of the sample preparation and curing treatment effects on mechanical properties and bioactivity of silica rich metakaolin geopolymer, Mater. Sci. Eng. C. 36 (2014) 20–24.
[8] C. Kuenzel, L. Li, L. Vandeperre, A.R. Boccaccini, C.R. Cheeseman, Influence of sand on the mechanical properties of metakaolin geopolymers, Constr. Build. Mater. 66 (2014) 442–446.
[9] Z. Peng, K. Vance, A. Dakhane, R. Marzke, N. Neithalath, Microstructural and 29Si MAS NMR spectroscopic evaluations of alkali cationic effects on fly ash activation, Cem. Concr. Compos. 57 (2015) 34–43.
[10] Y. Ma, J. Hu, G. Ye, The pore structure and permeability of alkali activated fly ash, Fuel. 104 (2013) 771–780.
[11] A.J. Katz, A.H. Thompson, Quantitative prediction of permeability in porous rock, Phys. Rev. B. 34 (1986) 8179–8181.
[12] A.J. Katz, A.H. Thompson, Prediction of rock electrical conductivity from mercury injection measurements, J. Geophys. Res. Solid Earth. 92 (1987) 599–607.
[13] B.F. Swanson, others, A simple correlation between permeabilities and mercury capillary pressures, J. Pet. Technol. 33 (1981) 2498–2504.
[14] S. Das, D. Stone, D. Convey, N. Neithalath, Pore- and micro-structural characterization of a novel structural binder based on iron carbonation, Mater. Charact. 98 (2014) 168–179.
[15] H. Ma, Z. Li, Realistic pore structure of Portland cement paste: experimental study and numerical simulation, Comput Concr. 11 (2013) 317–336.
[16] S. Igarashi, W. Chen, H.J.H. Brouwers, Comparison of observed and simulated cement microstructure using spatial correlation functions, Cem. Concr. Compos. 31 (2009) 637–646.
[17] T.S. Yun, K.Y. Kim, J. Choo, D.H. Kang, Quantifying the distribution of paste-void spacing of hardened cement paste using X-ray computed tomography, Mater. Charact. 73 (2012) 137–143.
[18] T. Ponikiewski, J. Katzer, M. Bugdol, M. Rudzki, X-ray computed tomography harnessed to determine 3D spacing of steel fibres in self compacting concrete (SCC) slabs, Constr. Build. Mater. 74 (2015) 102–108.
[19] K. Wan, Y. Li, W. Sun, Application of tomography for solid calcium distributions in calcium leaching cement paste, Constr. Build. Mater. 36 (2012) 913–917.
[20] S.R. Stock, N.K. Naik, A.P. Wilkinson, K.E. Kurtis, X-ray microtomography (microCT) of the progression of sulfate attack of cement paste, Cem. Concr. Res. 32 (2002) 1673–1675.
[21] E. Gallucci, K. Scrivener, A. Groso, M. Stampanoni, G. Margaritondo, 3D experimental investigation of the microstructure of cement pastes using synchrotron X-ray microtomography (μCT), Cem. Concr. Res. 37 (2007) 360–368.
[22] J.L. Provis, R.J. Myers, C.E. White, V. Rose, J.S.J. van Deventer, X-ray microtomography shows pore structure and tortuosity in alkali-activated binders, Cem. Concr. Res. 42 (2012) 855–864.

[23] W.R.L. da Silva, J. Němeček, P. Štemberk, Methodology for nanoindentation-assisted prediction of macroscale elastic properties of high performance cementitious composites, Cem. Concr. Compos. 45 (2014) 57–68.
[24] C. Hu, Z. Li, Micromechanical investigation of Portland cement paste, Constr. Build. Mater. 71 (2014) 44–52.
[25] G. Constantinides, F.-J. Ulm, The effect of two types of C-S-H on the elasticity of cement-based materials: Results from nanoindentation and micromechanical modeling, Cem. Concr. Res. 34 (2004) 67–80.
[26] L. Sorelli, G. Constantinides, F.-J. Ulm, F. Toutlemonde, The nano-mechanical signature of Ultra High Performance Concrete by statistical nanoindentation techniques, Cem. Concr. Res. 38 (2008) 1447–1456.
[27] J.D. Eshelby, The Determination of the Elastic Field of an Ellipsoidal Inclusion, and Related Problems, Proc. R. Soc. Lond. Math. Phys. Eng. Sci. 241 (1957) 376–396.
[28] T. Mori, K. Tanaka, Average stress in matrix and average elastic energy of materials with misfitting inclusions, Acta Metall. 21 (1973) 571–574.
[29] M. Hori, S. Nemat-Nasser, Double-inclusion model and overall moduli of multi-phase composites, Mech. Mater. 14 (1993) 189–206.
[30] D.P. Bentz, N.S. Martys, A Stokes permeability solver for three-dimensional porous media, US Department of Commerce, Technology Administration, National Institute of Standards and Technology Gaithersburg, MD, USA, 2007.
[31] M.S. Sumanasooriya, D.P. Bentz, N. Neithalath, Planar image-based reconstruction of pervious concrete pore structure and permeability prediction, ACI Mater. J. 107 (2010).
[32] K.J. Miller, W. Zhu, L.G.J. Montési, G.A. Gaetani, Experimental quantification of permeability of partially molten mantle rock, Earth Planet. Sci. Lett. 388 (2014) 273–282.
[33] K. Miled, K. Sab, R. Le Roy, Effective elastic properties of porous materials: Homogenization schemes vs experimental data, Mech. Res. Commun. 38 (2011) 131–135.
[34] G.K. Hu, G.J. Weng, The connections between the double-inclusion model and the Ponte Castaneda–Willis, Mori–Tanaka, and Kuster–Toksoz models, Mech. Mater. 32 (2000) 495–503.
[35] C.C. Yang, R. Huang, Double inclusion model for approximate elastic moduli of concrete material, Cem. Concr. Res. 26 (1996) 83–91.
[36] C.C. Yang, Approximate elastic moduli of lightweight aggregate, Cem. Concr. Res. 27 (1997) 1021–1030.
[37] W.R.L. da Silva, J. Němeček, P. Štemberk, Application of multiscale elastic homogenization based on nanoindentation for high performance concrete, Adv. Eng. Softw. 62–63 (2013) 109–118.
[38] J.J. Williams, Z. Flom, A.A. Amell, N. Chawla, X. Xiao, F. De Carlo, Damage evolution in SiC particle reinforced Al alloy matrix composites by X-ray synchrotron tomography, Acta Mater. 58 (2010) 6194–6205.
[39] F. De Carlo, B. Tieman, High-throughput x-ray microtomography system at the Advanced Photon Source beamline 2-BM, Proc. SPIE 5535 (2004) 644–651.
[40] B.A. Dowd, G.H. Campbell, R.B. Marr, V.V. Nagarkar, S.V. Tipnis, L. Axe, D.P. Siddons , Developments in synchrotron x-ray computed microtomography at the National Synchrotron Light Source, Proc. SPIE 3772 (1999) 224–236.
[41] M.L. Rivers, tomoRecon: High-speed tomography reconstruction on workstations using multi-threading, Proc. SPIE 8506 (2012) 85060U–85060U–13.
[42] F. Marone, M. Stampanoni, Regridding reconstruction algorithm for real-time tomographic imaging, J. Synchrotron Radiat. 19 (2012) 1029–1037.

[43] N. Bossa, P. Chaurand, J. Vicente, D. Borschneck, C. Levard, O. Aguerre-Chariol, et al., Micro- and nano-X-ray computed-tomography: A step forward in the characterization of the pore network of a leached cement paste, Cem. Concr. Res. 67 (2015) 138–147.
[44] M. Zhang, Y. He, G. Ye, D.A. Lange, K. van Breugel, Computational investigation on mass diffusivity in Portland cement paste based on X-ray computed microtomography (µCT) image, Constr. Build. Mater. 27 (2012) 472–481..
[45] P.J.M. Monteiro, A.P. Kirchheim, S. Chae, P. Fischer, A.A. MacDowell, E. Schaible, et al., Characterizing the nano and micro structure of concrete to improve its durability, Cem. Concr. Compos. 31 (2009) 577–584.
[46] H.Y. Moon, H.S. Kim, D.S. Choi, Relationship between average pore diameter and chloride diffusivity in various concretes, Constr. Build. Mater. 20 (2006) 725–732.
[47] R. Kumar, B. Bhattacharjee, Study on some factors affecting the results in the use of MIP method in concrete research, Cem. Concr. Res. 33 (2003) 417–424.
[48] E.J. Garboczi, D.P. Bentz, The effect of statistical fluctuation, finite size error, and digital resolution on the phase percolation and transport properties of the NIST cement hydration model, Cem. Concr. Res. 31 (2001) 1501–1514.
[49] W. C. Oliver, G. M. Pharr, Measurement of hardness and elastic modulus by instrumented indentation: Advances in understanding and refinements to methodology, J. Mater. Res. 19 (2004) 3–20.
[50] X. Li, B. Bhushan, A review of nanoindentation continuous stiffness measurement technique and its applications, Mater. Charact. 48 (2002) 11–36.
[51] N.R. Moody, W.W. Gerberich, N. Burnham, S.P. Baker, Fundamentals of nanoindentation and nanotribology, Warrendale, PA (United States); Materials Research Society, 1998.
[52] S.S. Singh, C. Schwartzstein, J.J. Williams, X. Xiao, F. De Carlo, N. Chawla, 3D microstructural characterization and mechanical properties of constituent particles in Al 7075 alloys using X-ray synchrotron tomography and nanoindentation, J. Alloys Compd. 602 (2014) 163–174.
[53] W. C. Oliver, G. M. Pharr, An improved technique for determining hardness and elastic modulus using load and displacement sensing indentation experiments, J. Mater. Res. 7 (1992) 1564–1583.
[54] A.E. Scheidegger, Physics of flow through porous media, in: Phys. Flow Porous Media, University of Toronto, 1963.
[55] J.L. Provis, J.S.J. Van Deventer, Geopolymers: structures, processing, properties and industrial applications, Elsevier, 2009.
[56] I. Garcia-Lodeiro, A. Palomo, A. Fernández-Jiménez, D.E. Macphee, Compatibility studies between NASH and CASH gels. Study in the ternary diagram Na 2 O–CaO–Al 2 O 3–SiO 2–H 2 O, Cem. Concr. Res. 41 (2011) 923–931.
[57] S.J. Cooper, D.S. Eastwood, J. Gelb, G. Damblanc, D.J.L. Brett, R.S. Bradley, et al., Image based modelling of microstructural heterogeneity in LiFePO4 electrodes for Li-ion batteries, J. Power Sources. 247 (2014) 1033–1039.
[58] S. Diamond, Mercury porosimetry: An inappropriate method for the measurement of pore size distributions in cement-based materials, Cem. Concr. Res. 30 (2000) 1517–1525.
[59] S. Diamond, Reply to the discussion by S. Wild of the paper “Mercury porosimetry—an inappropriate method for the measurement of pore size distributions in cement-based materials,” Cem. Concr. Res. 31 (2001) 1655–1656.
[60] M. Zalzale, P.J. McDonald, Lattice Boltzmann simulations of the permeability and capillary adsorption of cement model microstructures, Cem. Concr. Res. 42 (2012) 1601–1610.
[61] X. Sun, Q. Dai, K. Ng, Computational investigation of pore permeability and connectivity from transmission X-ray microscope images of a cement paste specimen, Constr. Build. Mater. 68 (2014) 240–251.

[62] P. Trtik, B. Münch, P. Lura, A critical examination of statistical nanoindentation on model materials and hardened cement pastes based on virtual experiments, Cem. Concr. Compos. 31 (2009) 705–714.
[63] G. Constantinides, K.S. Ravi Chandran, F.-J. Ulm, K.J. Van Vliet, Grid indentation analysis of composite microstructure and mechanics: Principles and validation, Mater. Sci. Eng. A. 430 (2006) 189–202.
[64] J. Němeček, V. Šmilauer, L. Kopecký, Nanoindentation characteristics of alkali-activated aluminosilicate materials, Cem. Concr. Compos. 33 (2011) 163–170.
[65] J. Němeček, V. Šmilauer, L. Kopeckỳ, Characterization of alkali-activated fly-ash by nanoindentation, in: Nanotechnol. Constr. 3, Springer, 2009: pp. 337–343.
[66] S. Das, M. Aguayo, G. Sant, B. Mobasher, N. Neithalath, Tensile Behavior in the Fracture Process Zone of Blended Binders Containing Limestone Powder, Cem. Concr. Res. 73 (2015) 51–62.
[67] B. Mobasher, V. Dey, Z. Cohen, A. Peled, Correlation of constitutive response of hybrid textile reinforced concrete from tensile and flexural tests, Cem. Concr. Compos. 53 (2014) 148–161.

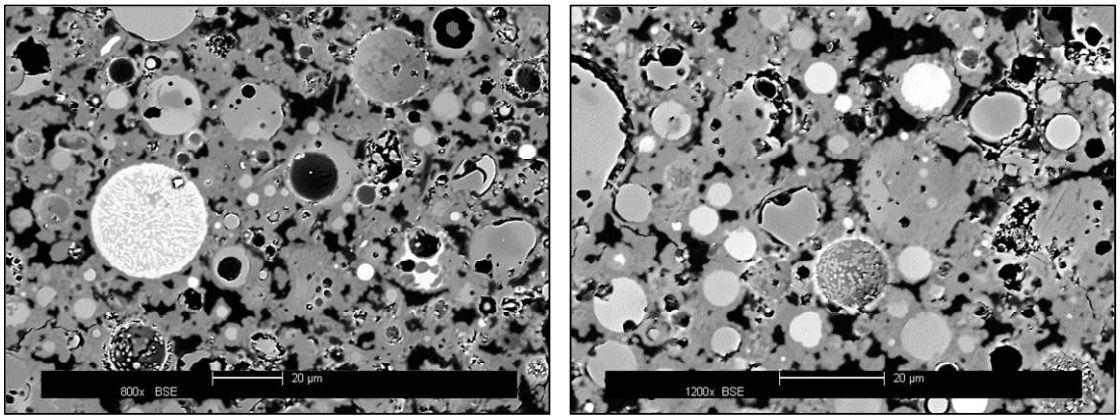

(a) **(b)**

Figure 1: Backscattered scanning electron micrographs of 8M NaOH activated fly ash after 2 days of heat curing at 60 °C: (a) lower (800X) and (b) higher (1200X) magnification. The scale bars correspond to 20 µm.

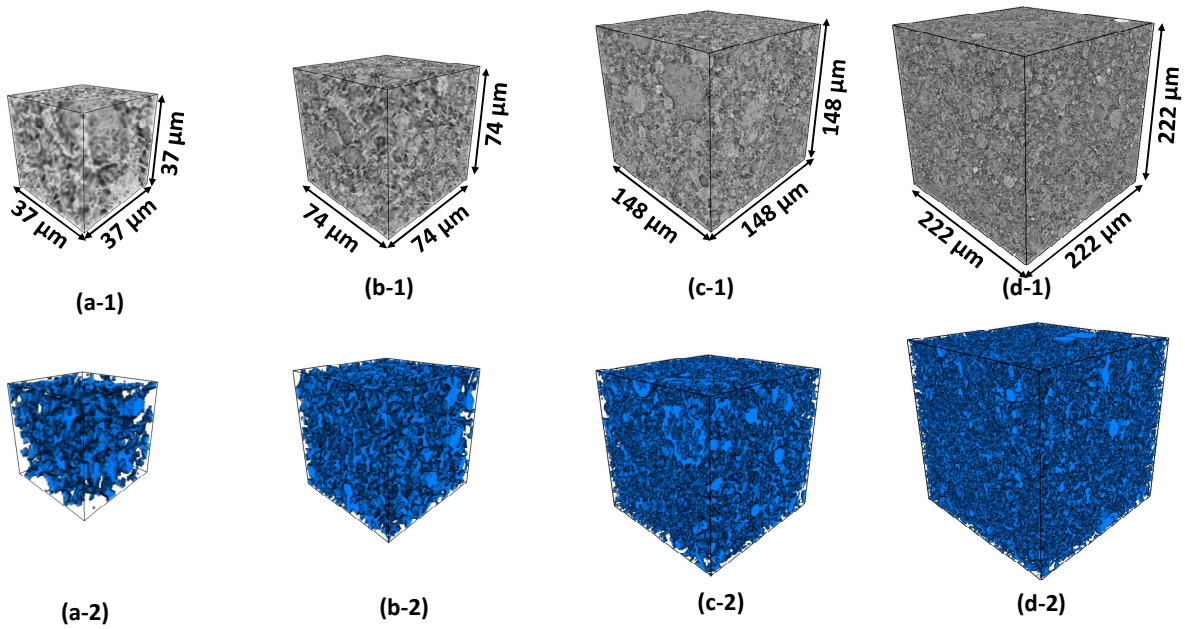

Figure 2: Representative microstructures of different sizes. Figures a1-d1 shows cubical volumes of interest extracted from the XRT dataset corresponding to 50^3, 100^3, 200^3, and 300^3 voxels respectively. Figures a2-d2 shows the segmented 3D pore structure corresponding to the above mentioned RVE sizes. Please refer to the online version of the paper for color images.

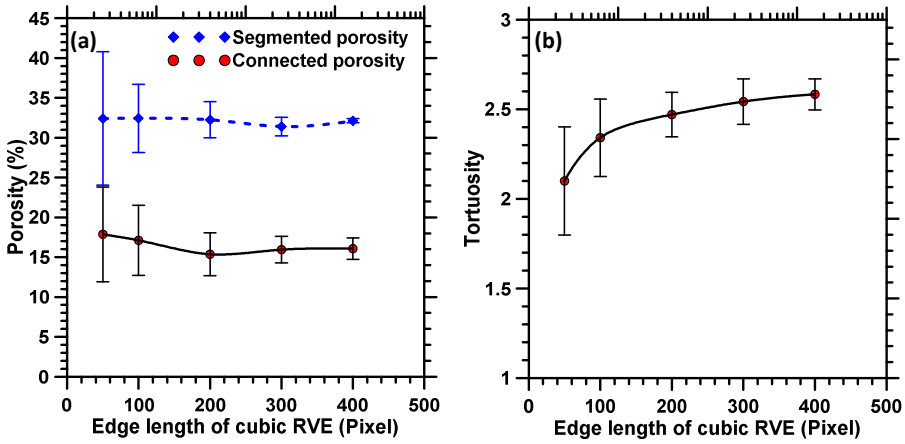

Figure 3: (a) 3D segmented (volumetric) and connected (percolated) porosities; (b) tortuosity as a function of the RVE size.

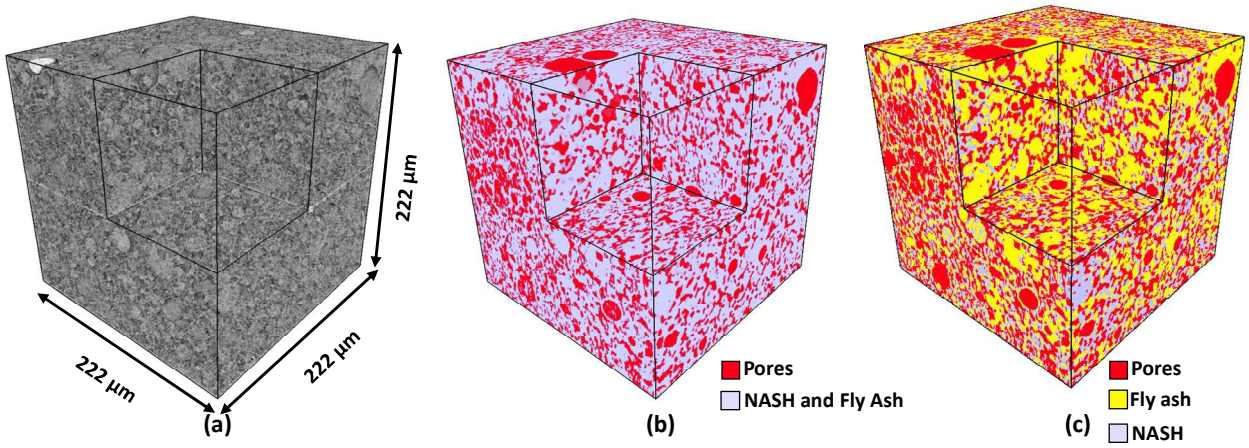

Figure 4: (a) Sequential, discrete thresholding implemented on a 300^3 voxel RVE obtained from XRT: (a) original XRT image, (b) 3D image after pore segmentation (two-phase; pore and solid), and (c) 3D image after further segmentation for two different solid phases (fly ash and N-A-S-H gel). Please refer to the online version of the paper for color images.

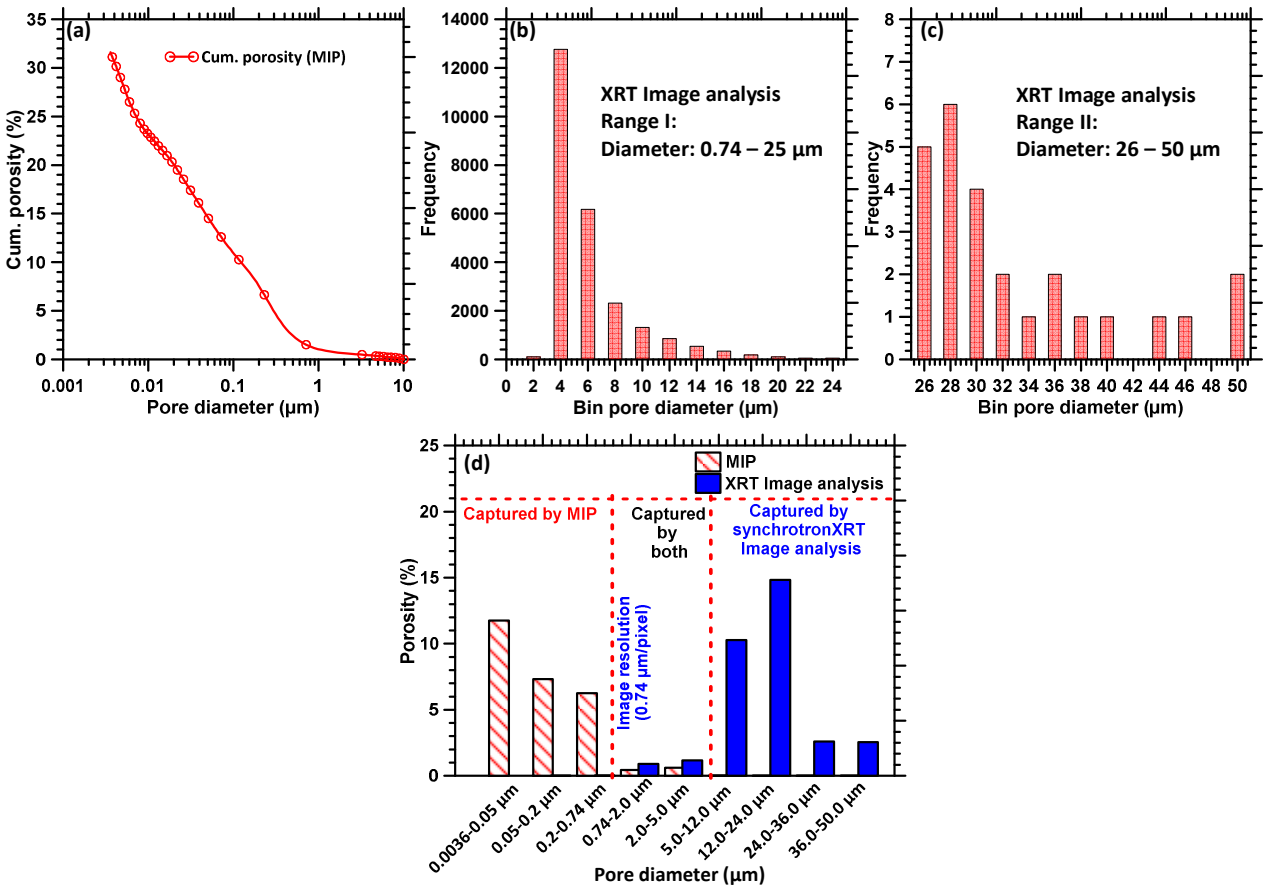

Figure 5: (a) Cumulative porosity-pore diameter relationship from MIP, (b) and (c) pore size distribution from 3D XRT in the range 0.74 µm-to-25 µm and 25 µm-to-50 µm respectively, and (d) comparison of pore sizes obtained using MIP and XRT techniques. For Figures (b) and (c), note that the Y-axes are different.

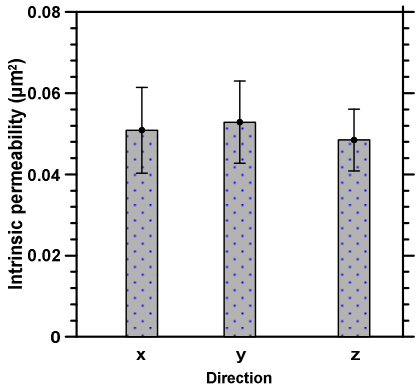

Figure 6: Intrinsic permeability in three orthogonal directions, computed using a numerical Stokes solver.

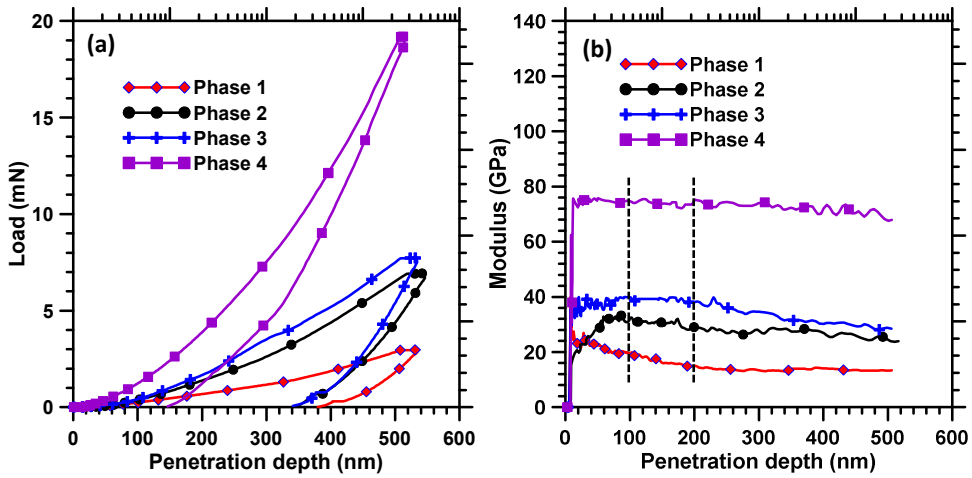

Figure 7: (a) Load-penetration depth curves for different phases in the fly ash-based geopolymer, and (b) Elastic modulus as a function of the penetration depth for the four distinct solid phases.

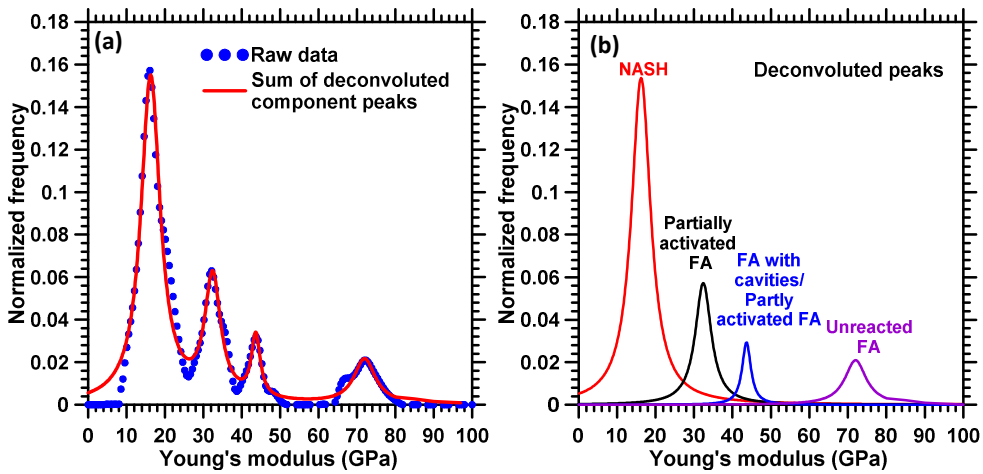

Figure 8: (a) Distribution of nanoindentation-based Young's modulus (raw data) in the fly ash-based geopolymer sample (symbols) and sum of deconvoluted component peaks (solid line), and (b) deconvoluted component peaks for the four distinctly identifiable microstructural phases in the solid component of the paste. The area under each deconvoluted peak is the fraction of that respective solid phase in all solids in the paste.

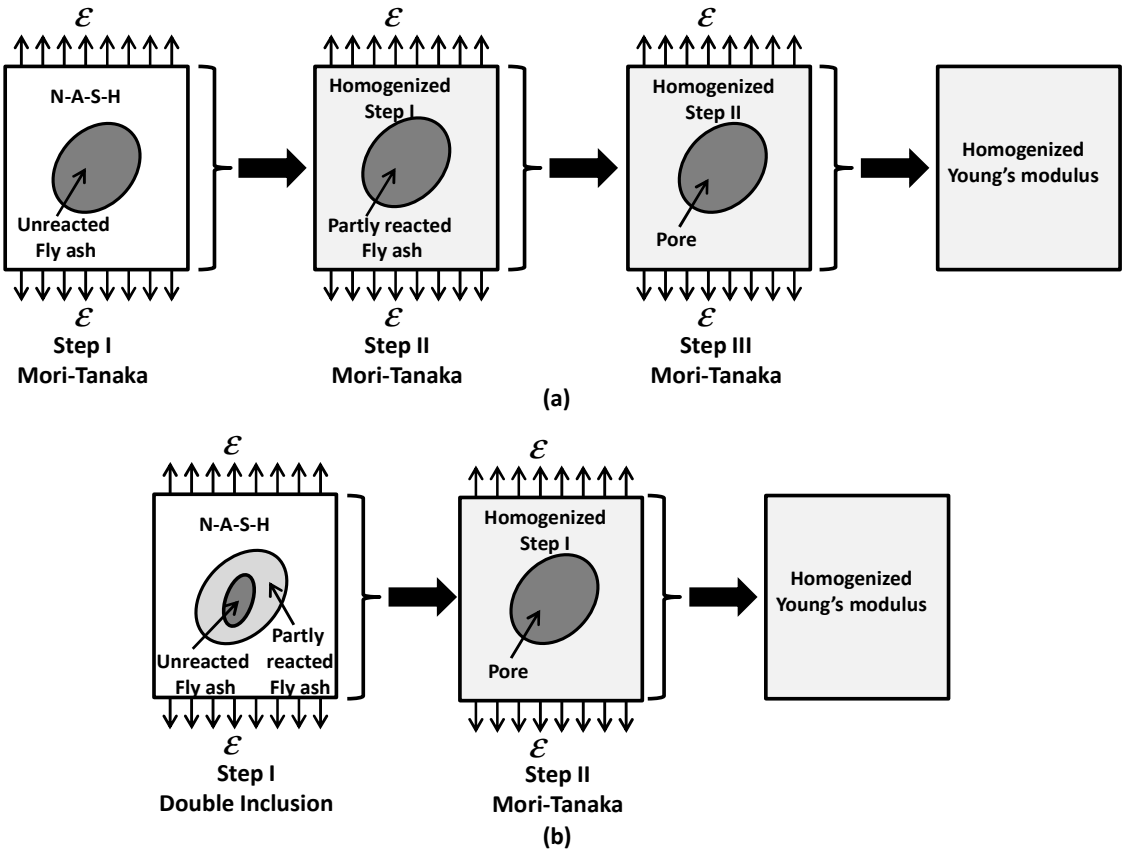

Figure 9: Schematic illustration of the homogenization process according to: (a) Mori-Tanaka method, and (b) double inclusion method

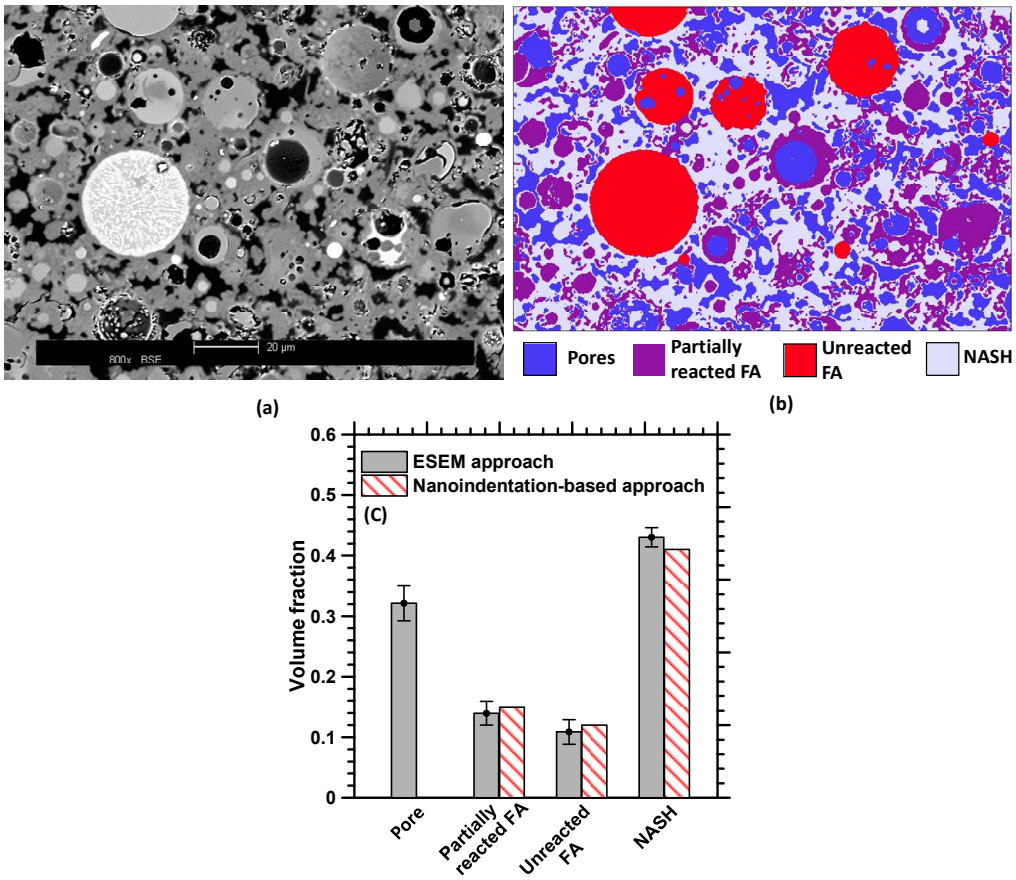

Figure 10: (a) Representative backscattered SEM of a fly ash-based geopolymer paste, (b) multi-phase threshold applied to the SEM image for phase identification and quantification, and (c) quantified volume fractions of different phases from SEM and the nanoindentation-based method. The scale bar in the SEM corresponds to 20 µm. Please refer to the online version of the paper for color images.